ChemElectroChem

Research Article
doi.org/10.1002/celc.202101197

Chemistry Europe
European Chemical Societies Publishing

Hematite as an Electrocatalytic Marker for the Study of Archaeological Ceramic Clay bodies: A VIMP and SECM Study**

Antonio Doménech-Carbó,*[a] Michele Giannuzzi,[b] Annarosa Mangone,[b, c] Lorena Carla Giannossa,[b, c] Francesca Di Turo,[d] Elena Cofini,[e] and María Teresa Doménech-Carbó[f]

The electrocatalytic effect exerted by hematite, a ubiquitous component of clay bodies, on the oxygen reduction reaction (ORR) and oxygen evolution reaction (OER) can be used to acquire information on archaeological ceramics. The solid-state voltammetric response of different hematite and ochre specimens, accompanied by SECM analysis in contact with 0.10 M HCl aqueous solution, is described. In air-saturated solutions, catalytic effects on the ORR and OER are accompanied by Fe(III)/Fe(II) and Fe(IV)/Fe(III) redox reactions. Such processes are conditioned by a variety of factors, the hydroxylation degree of the mineral surfaces being particularly influential, and exhibit significant variations upon heating the specimens between 300 and 900 °C. Voltammetric measurements carried out on a set of archaeological samples of Apulian red-figured pottery dated back within 5th and 4th centuries BCE permit to obtain site-characteristic voltammetric profiles.

Introduction

Recently, a great deal of attention has been paid to semiconducting materials as catalysts for different electrochemical processes.[1] Among other compounds, hematite (α-Fe_2O_3) has claimed attention as a photoanode for producing the oxygen evolution reaction (OER) because of its low cost, stability in contact with alkaline solutions, n-type semiconducting properties and band gap of around 2.0 eV. Processes catalyzed by hematite include oxygen reduction reaction (ORR),[2–5] photoelectrochemical water splitting,[6–11] and hydrogen peroxide oxidation.[12]

[a] Prof. Dr. A. Doménech-Carbó
Departament de Química Analítica
Universitat de València
Dr. Moliner, 50, 46100, Burjassot (València), Spain
E-mail: antonio.domenech@uv.es
[b] Dr. M. Giannuzzi, Prof. Dr. A. Mangone, Prof. Dr. L. C. Giannossa
Dipartimento di Chimica
Università degli Studi di Bari "Aldo Moro"
Via E. Orabona, 4, 70125 Bari, Italy
[c] Prof. Dr. A. Mangone, Prof. Dr. L. C. Giannossa
Centro Interdipartimentale Laboratorio di Ricerca per la Diagnostica dei Beni Culturali
Via E. Orabona 4, 70126 Bari, Italy
[d] Dr. F. Di Turo
National Enterprise for nanoScience and nanoTechnology (NEST)
Scuola Normale Superiore
Piazza dei Cavalieri 12, 56127 Pisa, Italy
[e] Dr. E. Cofini
Department of Earth Sciences
Sapienza University of Rome
P.le Aldo Moro 5, Rome, Italy
[f] Prof. Dr. M. T. Doménech-Carbó
Institut de Restauració del Patrimoni
Universitat Politècnica de València
Camí de Vera 14, 46022, València Spain

[**] VIMP = voltammetry of immobilized particles; SECM = scanning electrochemical microscopy

The electrochemistry of hematite has been widely studied. This compound, as well as other Fe(III) oxides and hydroxides, displays reductive dissolution processes in contact with acidic electrolytes.[13,14] On studying OER processes, it has been shown that the Fe(III) state in hematite can in principle be oxidized to any of the known higher oxidation states of iron (IV, V, and VI).[15–18] Then, the OER could involve not only formation of peroxo and superoxo species but also cycling of the oxidation state of Fe surface atoms.[15–18]

This rich electrochemistry is also of interest in the context of studies on ceramic materials and, in particular, archaeological pottery, in which hematite is a ubiquitous component. In this field, we have previously reported a series of works aimed to characterize the production from different archaeological sites using the voltammetry of immobilized particles (VIMP) methodology.[19–24] The VIMP is a solid-state electrochemistry technique developed by Scholz et al.[25,26] that yields analytical information on sparingly soluble solids.[27] Its capability to provide compositional and thermochemical information using sample amounts of only few nanograms makes VIMP an interesting technique for archaeometry, conservation and restoration,[28,29] including metal dating.[30] This technique can be intersected with electrochemical impedance spectroscopy (EIS),[21,22] a technique widely used to study metallic heritage,[31,32] and scanning electrochemical microscopy (SECM).[33]

Hematite is a component of pottery clay body materials which significantly contributes to their spectral properties.[34] These are, however, dependent on the crystallinity, particle size, degree of hydration Al^{3+} by Fe^{3+} substitution[34–37] of the hematite, properties which in turn are particularly sensitive to the mineral source and manufacturing of pottery. Ultimately, this deals with a crucial problem in archaeology: the elucidation of the techniques of fabrication of ceramic materials.[38–40] Here,

we explore: i) the electrocatalytic effects on OER and ORR processes exerted by hematite minerals with different crystallinity and degree of hydration, ii) the exploitation of such effects to characterize archaeological pottery. Voltammetric data are complemented with field emission scanning electron microscopy (FESEM) and SECM.

The electrochemistry of hematite minerals is compared with that displayed by microsamples from Apulian red-figured pottery from four archaeological sites (Altamura, Arpi, Monte Sannace and Taranto, Apulia, Italy). This type of pottery, produced within 5th and 4th centuries BCE, widely spread and marketed both within and outside of the Apulian region, has received considerable attention due to its excellent quality.[41,42] There is debate, however, about its relation with the preceding Attic production and the development of local technologies, so that discrimination between different archaeological sites and techniques is of great interest.[43–45]

Experimental Section

Electrochemical experiments were performed at microparticulate deposits of the ceramic samples and reference materials. These were anhydrous, crystalline Fe_2O_3 (Carlo Erba) (in the following, H0) and different hematite-containing red pigments (Natural hematite Kremer 48600 (H1), Spanish hematite, Kremer 48651 (H2), Erculano red, Kremer 41600 (H3)) and three orange to yellow ochre pigment (French ochre Kremer 40030 (O1), 40040 (O2) and 40050 (O3)). Electrode modification was carried out either by evaporation at air of a drop (50 μL) of an ethanolic suspension (1 mg mL^{-1}) of the solid onto the surface of a glassy carbon electrode (GCE) (BAS MF 2012, geometrical area 0.071 cm^2) or abrasively transferred onto graphite electrodes (Alpino Maxim HB-type, 2 mm diameter) as usual in VIMP technique.[25,26] Prior to modification, GCEs were cleaned with piranha solution for 24 h, rinsed with water and electrochemically cleaned/activated by cycling the potential between 1.25 and −1.25 V in air-saturated 0.10 M HCl at 500 mV s^{-1} until constant response. Aqueous 0.1 M HCl solutions, optionally deaerated by bubbling Ar during 10 min, were used as electrolytes. Voltammetric measurements were performed in a conventional three-electrode cell using a Ag/AgCl (3 M NaCl) reference electrode and a Pt-wire auxiliary electrode using a CH I660 (Cambria Scientific, Llwynhendy, Llanelli UK) potentiostat. SECM experiments were carried out on a CH 920c equipment preparing microparticulate deposits of minerals and ceramic pastes onto a bed of carbon paste (30% graphite powder plus 70% paraffin oil) covering a Pt electrode. Air-saturated 0.10 M HCl was used as the electrolyte in order to use the ORR process as the redox probe.[31] The Pt tip microelectrode (25 μm diameter) was accompanied by Ag/AgCl (3 M NaCl) reference and a Pt-wire auxiliary electrodes. Experiments were carried out based on the redox competition methodology[46] applying different potential inputs to the tip and the substrate electrode. FESEM images were obtained with a S-4800 Hitachi equipment (Hitachi Ltd., Tokyo, Japan) on carbon-coated mineral samples operating at 1–20 kV. The microanalysis of samples was performed with the associated energy dispersive X-ray microanalysis system (SEM/EDX).

Firing experiments were carried out by heating in furnace aliquots of 0.20 g of H0-H3 and O1-O3 specimens placed in porcelain containers for 24 h. Temperatures between 300 and 900 °C were tested. After heating, the samples were stored for 15 min in a dessicator and then VIMP experiments were carried out.

Ceramic samples from Apulian vases were conducted on slivers (few square millimeters) taken from already existing fractures or at the edges of the fragment. These were 13 from Monte Sannace (MS1, M8, M9, M14, M25, M28, M29, M31, AM2, AM3, AM4, AM6, AM7), 5 from Altamura (A4, A5, A8, A9, and A11), 10 from Arpi (I1-01, I2-01, I3-01, C1-01, C7-01, A1-01, F-01, Ar4, Ar5, C5), and 15 from Taranto (212411, 227007, 227093, 227130, 227141, 227161, 227183, 227185, 227186, 227197, 227204, 227229, 227236, 227237, and 52231B).

Results and Discussion

Voltammetric Pattern

Figure 1a,b shows the cyclic voltammograms (CVs) at H0 hematite-modified GCE in contact with deoxygenated 0.10 M HCl aqueous solution. In the initial cathodic scan (Figure 1a), an ill-defined cathodic wave appears at ca. −0.7 V (C_H) preceding the rising current for hydrogen evolution reaction (HER) which is clearly enhanced relative to that recorded at the unmodified GCE. In the subsequent anodic scan, a weak shoulder appears at ca. −0.6 V, preceding an oxidation wave at 0.8 V (A_{HE}) ending with the rising current for the oxygen evolution reaction (OER). This current is significantly increased respect to the unmodified GCE. In the subsequent cathodic scan, a weak signal C_{HE} coupled to the A_{HE} wave appears. In the initial anodic scan voltammograms (Figure 1b), the signal A_{HE} is absent, being only recorded in the second and subsequent scans.

In air-saturated solutions (Figure 1c, d) the voltammetric pattern was dominated by the prominent cathodic wave for the reduction of dissolved oxygen (C_{ORR}) ca. −0.65 V. This signal is significantly enhanced relative to that recorded at unmodified electrodes and masks the C_H signal. In turn, the A_H wave at 0.8 V becomes enhanced, also appearing, as before, only after the previous cathodic run. These features denote that the species

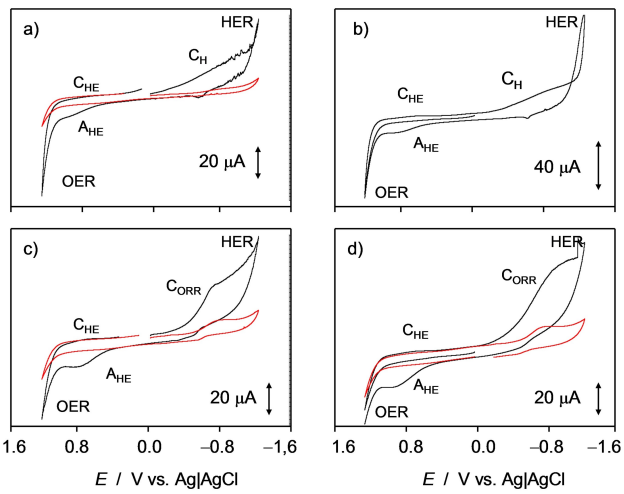

Figure 1. CVs at H0 hematite-modified GCE (black) and unmodified GCE (red) in contact with a, b) deoxygenated and c, d) air-saturated 0.10 M HCl aqueous solution. Potential scan initiated at 0.0 V in the a, c) negative and b, d) positive direction; potential scan rate 50 mV s^{-1}.

responsible for the peak A_H is electrochemically generated in previous cathodic processes.

The C_H signal can be attributed, according to literature,[13,14,19] to the reductive dissolution of hematite. This process, that is only relevant at strongly acidic pHs, is generally represented by the equation (1):

$$Fe_2O_3 + 6\ H^+_{aq} + 2\,e^- \rightarrow 2\ Fe^{2+}_{aq} + 3\ H_2O \quad (1)$$

Under our experimental conditions, the process C_H can involve a more complex pathway as suggested by the peak splitting observed in negative-going potential scan square wave voltammograms (SWVs) such as in Figure 2. These features can be interpreted as resulting from the heterogeneity in the shape and size distribution of hematite particles,[13,14] but also from the superposition of different electrochemical pathways. Interestingly (vide infra), the signal C_{HE} appears well-defined, although weak, in SWVs initiated at potentials ca. 1.0 V (Figure 2).

In air-saturated HCl solutions (Figure 1c,d), the process C_H is superimposed to the gross cathodic wave corresponding to the ORR process. According to Compton et al.,[4] in neutral media, hematite acts as a chemical catalyst accelerating the disproportionation of H_2O_2 into H_2O and O_2 during the ORR process at GCEs. In alkaline media, Wang et al.[5] have reported that partial reduction of hematite nanoplates activate them as electrocatalysts for ORR and that magnetite (Fe_3O_4) plus hematite composites offer the higher catalytic performance. The "chemical" catalytic cycle for ORR[4] is schematized in Figure 3a. The process is initiated by the one-electron reduction of O_2 to superoxide radical anion further yielding H_2O_2. Then, hematite catalyzes the disproportionation of H_2O_2 into H_2O and O_2, the regeneration of O_2 accelerating the overall ORR process.

Under the acidic conditions used here, it seems conceivable that there is possibility of a second electrocatalytic pathway which refers to the electron-Fenton and Haber-Weiss reactions involving a solid catalyst. This pathway, that would operate superimposed to the above, involves the hematite reduction

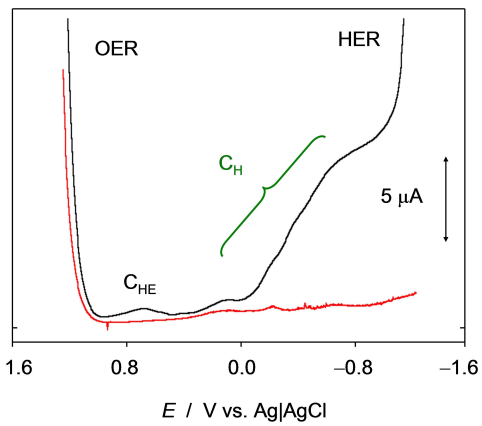

Figure 2. SWVs at H0 hematite-modified GCE (black) and unmodified GCE (red) in contact with deoxygenated 0.10 M HCl aqueous solution. Potential scan initiated at 1.25 V in the negative direction; potential step increment 4 mV; square wave amplitude 25 mV; frequency 10 Hz.

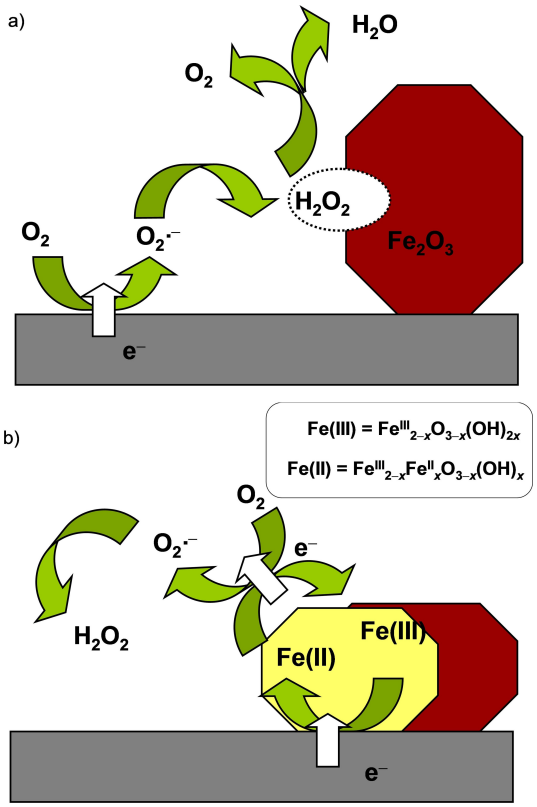

Figure 3. a) Scheme for the chemical hematite catalysis on the ORR process. Here, O_2 is reduced to $O_2^{\bullet-}$, further protonated to H_2O_2 whose disproportionation into O_2 and H_2O is catalyzed by hematite.[4] b) Tentative scheme for the electrocatalytic ORR process mediated by hydroxylated hematite forms. Here, Fe(III) hematite surface sites are electrochemically reduced to Fe(II) ones. These transfer one electron to O_2 yielding $O_2^{\bullet-}$, thus accelerating the first step of the ORR process, the Fe(II) catalyst being electrochemically regenerated. The intermediate steps yielding H_2O_2 from $O_2^{\bullet-}$ are omitted for simplicity.

generating surface Fe(II) active sites at potentials near to those where the ORR process occurs. This can be represented as equation (2):

$$Fe_2O_3 + x\ H^+_{aq} + x\ e^- \rightarrow Fe^{III}_{2-x}Fe^{II}_xO_{3-x}(OH)_x \quad (2)$$

These active sites can react with O_2 generating superoxide radical anion, thus accelerating the first step of the electrochemical ORR process that yields $O_2^{\bullet-}$ [Eq. (3)]:

$$Fe^{III}_{2-x}Fe^{II}_xO_{3-x}(OH)_x + x\ H_2O + O_2 \rightarrow Fe^{III}_2O_{3-x}(OH)_{2x} + x\ H^+_{aq} + O_2^{\bullet-} \quad (3)$$

The produced superoxide radical anion can then experience the subsequent chemical/electrochemical steps yielding H_2O_2 and H_2O. The catalytic Fe(II) centers are electrochemically regenerated within the same potential range via the process, equation (4):

$$Fe^{III}{}_2O_{3-x}(OH)_{2x} + x\ H^+{}_{aq} + x\ e^- \rightarrow Fe^{III}{}_{2-x}Fe^{II}{}_xO_{3-x}(OH)_x + x\ H_2O \quad (4)$$

thus completing an electrochemical catalytic cycle for the ORR process. This second pathway is schematized in Figure 3b. Notice that, in agreement with extensive VIMP literature,[25–28] the electrochemical Fe(III) to Fe(II) reduction will occur near the hematite/base electrode/electrolyte three-phase boundary. The proposed catalytic pathway agrees with the classical reaction/electrochemical regeneration scheme characterizing solution-phase electrocatalysis replacing the electrolyte catalyst by the solid-state catalyst attached to the electrode.

Under the acidic conditions used here, the hematite surface can be protonated (isoelectric pH 8.4–8.5) so that the hydroxylated Fe(III) species will be stable. The reactivity of these hydroxylated species can differ from that of anhydrous hematite. In fact, it has been reported that surface hydroxylation of hematite influences notably its structure and reactivity.[47] Then, the anodic process A_{HE} can be attributed to the oxidation of the electrochemically generated hydoxylated hematite species. This process can be represented by the equation (5):

$$Fe^{III}{}_2O_{3-x}(OH)_{2x} \rightarrow Fe^{III}{}_{2-x}Fe^{IV}{}_xO_3(OH)_x + 2x\ H^+ + 2x\ e^- \quad (5)$$

This is consistent with the infrared spectroscopy study from Zandi and Hamann[48] who proposed that an iron-oxo ($Fe^{IV}O$) species generated in the hydroxyl oxidation on the hematite surface is involved in water splitting. This proposal is consistent with cyclic voltammetry and potential modulated absorption spectroscopy reported by Cummings et al.[16,17] Generically, the Fe(III) to Fe(IV) oxidation can be represented as equation (6):[16,17,48]

$$Fe^{III}{-}OH \rightarrow Fe^{IV} = O + H^+ + e^- \quad (6)$$

Additionally, hematite forms can be oxidized at the potentials where the OER process occurs. Li et al.[49] have recently reported that surface hydroxylated hematite promotes photoinduced hole transfer for water oxidation in alkaline media whereas Le Formal et al,[15] have suggested that hole generation and the formation of Fe(V)-oxo species under strongly alkaline conditions and strong anodic bias are involved in photochemical OER. Formally, the electrochemical oxidation of anhydrous hematite can be represented as equation (7):

$$Fe^{III}{}_2O_3 + 2x\ H_2O \rightarrow Fe^{IV}{}_xFe^{III}{}_{2-x}O_3(OH)_{2x} + 2x\ H^+ + 2x\ e^- \quad (7)$$

Accordingly, the process C_{HE} recorded when the potential is scanned in the negative direction starting from potentials around those producing the OER process (Figure 2) can be assigned to the reduction of these hydroxylated Fe(IV) forms.

Interestingly, the voltammetry of anhydrous, crystalline hematite differs from that recorded for hydrated forms. This can be seen in Figure 4, where the CVs for a) anhydrous, crystalline hematite, and b) hydroxylated hematite pigment H1, in contact with air-saturated 0.10 M HCl are depicted. Consistently with the above considerations, hydroxylated hematites (Figure 4b) display C_{HE} signals larger than that of anhydrous hematite (Figure 4a). This is particularly relevant for the study of ceramic clay materials. Although these are constituted by a variety of materials (silicates, aluminosilicates, oxides, etc.) with different degree of hydration and crystallinity, only the iron compounds, hematite forms in particular, are significantly electroactive under our experimental conditions.

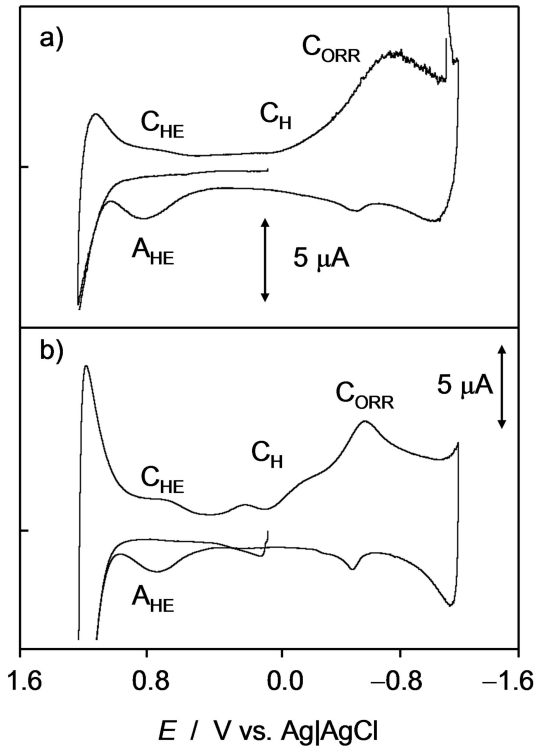

Figure 4. CVs of GCEs modified with CVs for a) anhydrous, crystalline hematite (H0), and hematite H1, in contact with air-saturated 0.10 M HCl aqueous solution. Potential scan initiated at 0.0 V in the positive direction; potential scan rate 50 mV s^{-1}.

Figure 5 compares the square wave voltammetric (SWV) response of microparticulate deposits of a) crystalline hematite (chemical reagent), b) hematite pigment H1, and ceramic samples c) A5 (Altamura) and d) 212411 (Taranto) onto graphite electrodes in contact with air-saturated 0.10 M HCl aqueous solution. The use of graphite electrodes was motivated by the need of processing a relatively large number of ceramic samples avoiding the time-consuming repeated cleaning of GCEs.

The voltammograms, limited by the OER and HER currents, show peaks at 0.8 V (C_{HE}), 0.4 (C_g) and −0.15 V (C_H) preceding the ORR peak at ca. −0.70 V (C_{ORR}). The signal C_g can be assigned to redox processes involving oxygen functionalities in the graphite surface,[50,51] as denoted by blank experiments in the absence of modifier.

One can see in Figure 5 that all voltammograms exhibit a similar pattern although differing in the relative height of the signals, in particular of the A_H and C_{ORR} ones (respectively $I(C_{HE})$,

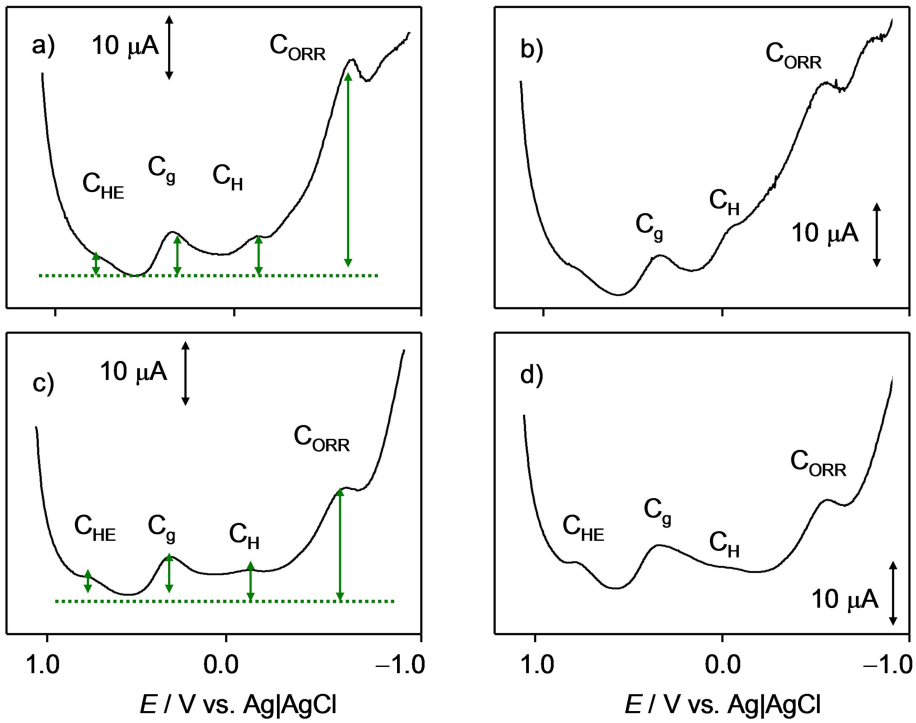

Figure 5. SWVs at graphite electrodes modified with a) anhydrous hematite (H0), b) hematite H1, and ceramic samples c) A5 (Altamura) and d) 212411 (Taranto) in contact with air-saturated 0.10 M HCl aqueous solution. Potential scan initiated at 1.25 V in the negative direction; potential step increment 4 mV; square wave amplitude 25 mV; frequency 5 Hz. Dotted lines represent the base lines used for peak current measurements.

$I(C_{ORR})$). Noticeably, i) the signal C_{HE} decreases or entirely vanishes for ochre-type pigments, thus denoting that this process is attributable to hematite forms; ii) the signal C_{ORR} is higher for crystalline hematite than for hematite-containing pigments. These features suggest that enhancing the degree of hydration and/or lowering the crystallinity of hematite decreases the catalytic effect on the ORR process. Other factors that influence the voltammetric response of iron oxide minerals, such as Al^{3+} by Fe^{3+} substitution,[52] will decrease the catalytic ability of hematite towards ORR.

Scanning Electrochemical Microscopy

As previously noted, our data suggest that the signal C_{ORR} (including the occluded signal C_H) recorded in air-saturated solution is representative of the content of anhydrous, crystalline hematite in the ceramic material whereas the signal A_H is representative of the content in hydrated iron oxide forms. This scenario was tested by SECM experiments.

Figure 6 compares the SECM color plots (a, b) and the corresponding topographic SECM images (c, d) obtained for a microparticulate deposit of crystalline hematite fixed onto a carbon paste bed in contact with air-saturated 0.10 M HCl. In these experiments the tip potential (E_T) was fixed at −0.65 V in order to use the reduction of dissolved oxygen as a redox probe, while different substrate potentials (E_S) were applied to the hematite particles. According to the redox competition methodology,[46] the variations in the tip current will reflect the changes in the conductivity, topography, and electroactive properties of the substrate.

When no potential inputs were applied to the hematite microparticles substrate, the mineral grains appear as positive feedback features in agreement with the catalytic effect exerted on the ORR process detected by the tip (Figure 6a, c). When a potential cathodic enough to promote/reinforce the ORR process (−0.70 V) is applied to the substrate (Figure 6b, d), the SECM pattern becomes slightly changed, the unique relevant features being a small narrowing of the hematite grains and the disappearance of several small crystals. These features can be considered as consistent with the previously discussed superposition of the reductive hydroxylation (Eq. (2)) and the reductive dissolution (Eq. (1)) of hematite grains.

Comparable SECM patterns were obtained for ceramic samples. Figure 7 depicts the color plots (a) and topographic SECM image (b) obtained for a microparticulate deposit of ceramic sample I1-01 (Arpi) in contact with air-saturated 0.10 M HCl, again fixing $E_T = -0.65$ V, when no potential input is applied to the substrate. Here, the ceramic grains appear as positive feedback features in principle associated to the electrocatalytic effect exerted by hematite on the ORR probe.

Reproducing the voltammetric pattern in Figure 1, the substrate potential was successively fixed to −0.70 V and 1.0 V. When a potential of −0.70 V was applied to the substrate (c), a significant number of the above positive feedback features vanish. This can be interpreted as a result of the more easy reductive dissolution of hydrated, less-crystalline hematite forms, as observed in minerals and pigments.[52,53] As a result,

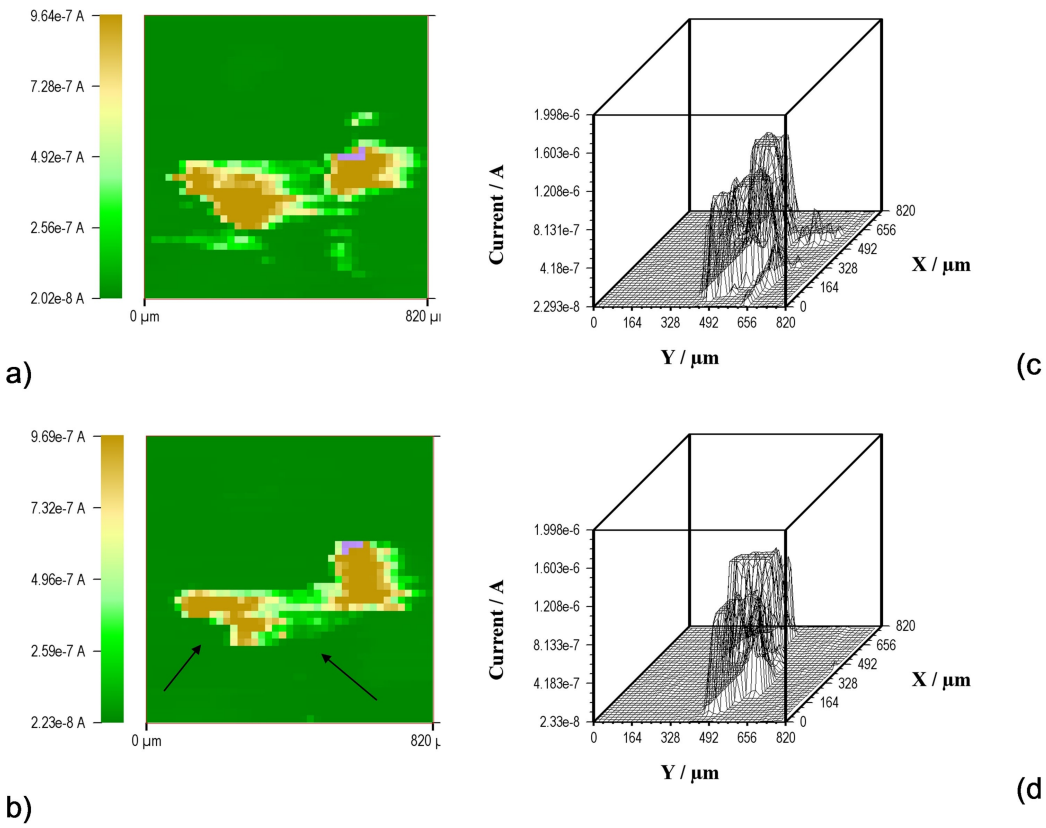

Figure 6. a, b) SECM color plots and c, d) topographic SECM profiles of a microparticulate deposit of crystalline hematite fixed onto a carbon paste bed in contact with air-saturated 0.10 M HCl. The tip potential was fixed at −0.65 V; substrate potential a, c) 0.0 V; b, d) −0.70 V.

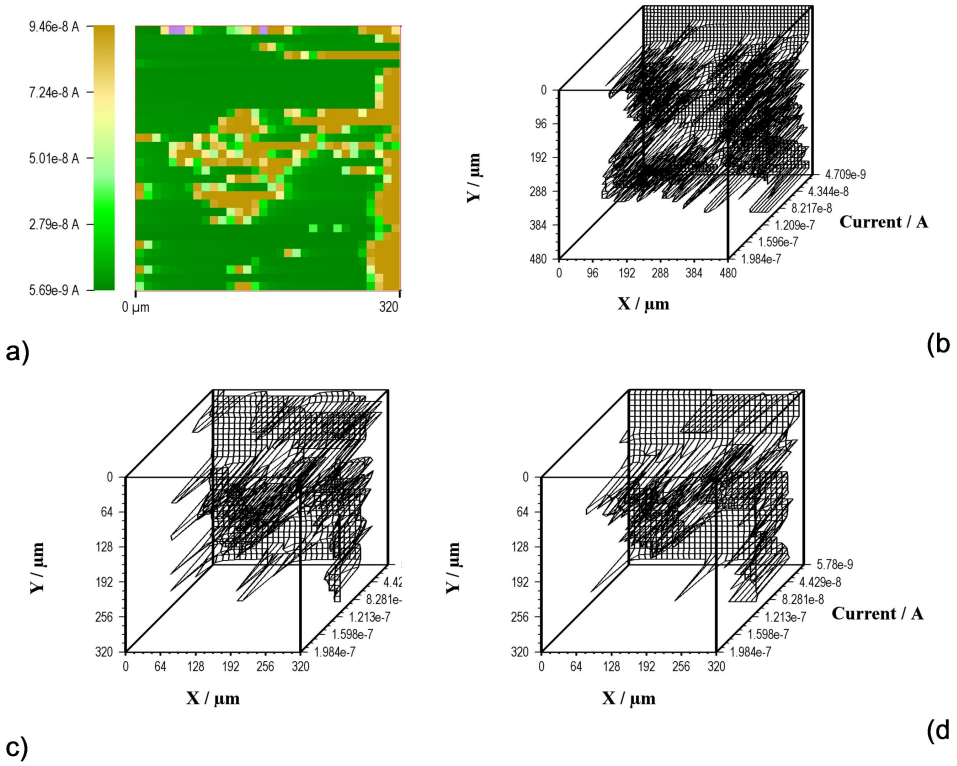

Figure 7. a) SECM color plot and b–d) topographic SECM profile of a microparticulate deposit of ceramic sample I1-01 (Arpi) fixed onto a carbon paste bed in contact with air-saturated 0.10 M HCl. $E_T = -0.65$ V; E_S was successively fixed from 0.0 V (a, b) to −0.70 V (c) and 1.0 V (d).

the net amount of crystalline hematite decreases and the density of positive feedback features lowers. When a potential of 1.0 V is applied to the substrate (d), several of the above peaked features remain while any other disappear. Since this potential is sufficiently positive to oxidize the hydroxylated Fe(III) surface species (Eq. (5)) presumably formed during the previous cathodic step, the above features suggest that there is no regeneration of anhydrous hematite producing positive feedback outputs at the tip.

Modeling Voltammetry of Immobilized Particles

Since in VIMP experiments under our experimental conditions there is no possibility of determining the net amount of sample transferred onto the graphite surface, the relative intensity of the voltammetric peaks rather than their individual values has to be used for quantitative purposes.

Figure 8 depicts the plots of $I(C_{ORR})$ vs. $I(C_{HE})$ for crystalline hematite and hematite pigments H1 and H3 in replicate experiments such as in Figure 5. In spite of relatively high dispersion, one can see that: i) the experimental data points appear to define linear tendency graphs and ii) the $I(C_{ORR})/I(C_{HE})$ ratio for crystalline hematite is larger than that for hydrated, less-crystalline forms. This feature is consistent with the electrocatalytic pathway proposed by Compton et al.[4] where hematite accelerates the decomposition rate of hydrogen peroxide, the intermediate product in the ORR process. As previously noted, this process will be less favored for hydrated, less-crystalline forms and/or Al^{3+} by Fe^{3+} substitution, etc. On the contrary, the oxidation of hematite (A_{HE}/C_{HE} process) appears to be scarcely sensitive to hydration degree and crystallinity as evidenced by the similarity in the $I(C_{HE})$ values for different minerals and pigments.

The apparent linear tendencies in Figure 8 can be interpreted on considering that the hematite forms a discontinuous microparticulate deposit onto the graphite surface. According to the theoretical description of redox processes under VIMP conditions due to Lovric, Scholz, Oldham and coworkers,[54–57] the redox reaction initiates at the particle/base electrode/electrolyte three-phase junction. In the case of electrocatalysis on ORR, the measured peak currents will ideally be composed of the sum of the contributions of the non-catalytic process occurring at the exposed graphite surface and the catalytic one localized in the hematite grains/graphite/electrolyte boundary. The second will be proportional to the perimeter of the three-phase junction (and hence, to the surface covered by hematite particles, S) while the former will be proportional to the non-covered graphite surface. Then the peak current (I_J) for the electrochemical process J (J = H, OER, ORR, etc.) can be expressed as equation (8):

$$I_J = g_J(S_o - S) + ph_J S \tag{8}$$

where S_o represents the total area of the graphite electrode, g_J, h_J, the electrochemical coefficient of response of the J-process at the graphite surface and the catalytic process, respectively. p represents a geometrical coefficient relating the surface of the hematite particles with their perimeter. In VIMP replicate experiments for a given hematite-containing material, S will vary while the other parameters can be roughly approximated by constants. Then, combining the equations for two electrochemical processes A and B, one obtains equations (9) and (10):

$$\frac{I_A - g_A S_o}{ph_A - g_A} = \frac{I_B - g_B S_o}{ph_B - g_B} \tag{9}$$

$$I_B = I_A\left(\frac{ph_B - g_B}{ph_A - g_A}\right) + S_o\left(g_B - g_A\frac{ph_B - g_B}{ph_A - g_A}\right) \tag{10}$$

Equation (10) predicts linear I_B vs. I_A variations in which the slope and ordinate at the origin will be characteristics of each mineral or ceramic material. This treatment, however, has to be viewed as an extremely simplified approximation. Due to the abrasive character of the transference of the mineral sample, the graphite surface suffers scratching resulting not only in the variation of the area S_o but also on the number of graphite sites (edges, planes) having different electroactivity. These factors will determine the relatively high data dispersion in representations such as in Figure 8.

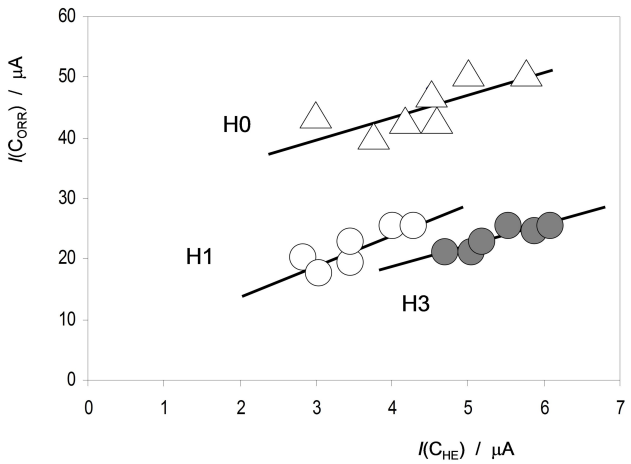

Figure 8. Plots of $I(C_{ORR})$ vs. $I(C_{HE})$ for crystalline hematite (H0) and hematite pigments H1 and H3 in replicate SWV experiments at sample-modified graphite electrodes immersed into air-saturated 0.10 M HCl in conditions such as in Figure 5.

Firing Temperature

We also studied the effect of firing temperatures between 300 and 900 °C on the voltammetric behavior of the different hematite and ochre materials. The results are condensed in Figure 9, where the average values of the $I(C_{HE})/I(C_{ORR})$ ratio are plotted vs. the firing temperature. On first examination, one can expect that, upon heating, the response of hydroxylated materials was approaching that of anhydrous hematite H0. However, our data revealed a smooth increase of the $I(C_{HE})/$

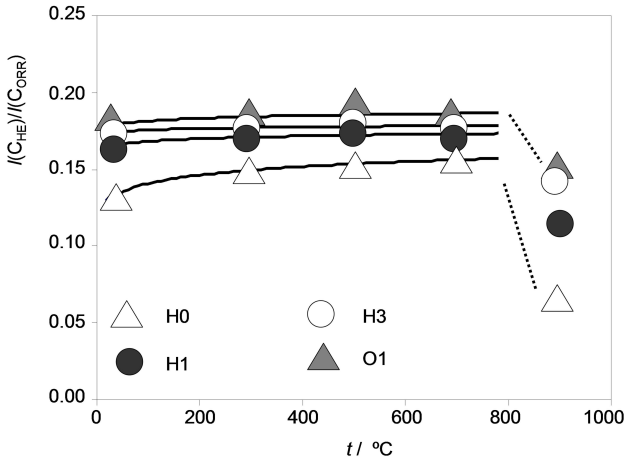

Figure 9. Plots of $I(C_{ORR})/I(C_{HE})$ vs. temperature in firing experiments. From SWVs such as in Figure 5 for H0, H1, H3 and O1 specimens.

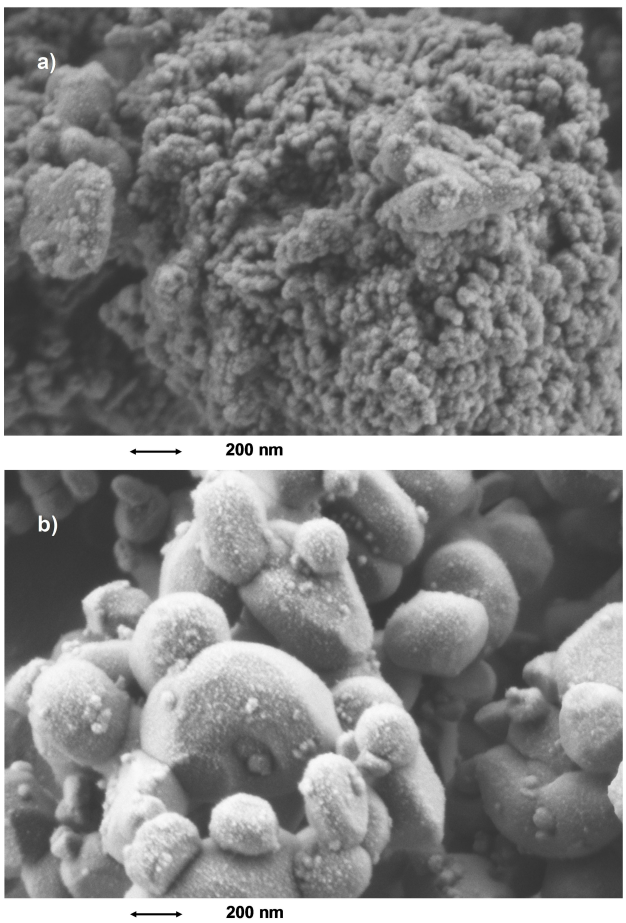

Figure 10. FESEM images recorded at 1 kV of carbon-coated samples of natural hematite pigment (sample H1) a) before and b) after heating at 900 °C for 24 h.

$I(C_{ORR})$ on increasing temperature between 300 and 700 °C, followed by an abrupt decrease at ca. 900 °C.

Interestingly, FESEM images denoted a significant morphological change in hematite specimens above 900 °C. Figure 10 illustrates the corresponding images for natural hematite pigment (sample H1) before and after heating at 900 °C for 24 h. The original pigment is constituted by aggregates of irregular microcrystals forming dense rough surfaces with features around 20–50 nm sized. After heating at 900 °C the image shows spheroidal crystals 500–800 nm sized.

These results can be correlated with literature reports on the thermal conversion of goethite (FeO(OH)) into hematite,[34–37] and density functional theory (DFT) calculations on dehydroxylation of hematite surfaces.[47–49] At temperatures between 250 and 600 °C, lath-like hematite crystals are formed without significant alteration of the shape and size of the parent goethite crystals. The infrared spectra of these specimens differ from those of hematite crystals formed between 700 and 950 °C where interparticle sintering processes occur.[37] The FESEM images in Figure 10 can be interpreted assuming that the surface of the parent hematite crystals contains hydrated/hydroxylated features that are removed at high temperatures accompanied by crystal sintering. In fact, the DFT theoretical study of Guo and Barnard[47] concluded that depending on the supersaturation of water and oxygen, {100} hematite surfaces can acquire variable hydroxylation status. In water-rich environments, these can involve chemisorbed water molecules, the hydrogenation of undercoordinated subsurface oxygen atoms, and the formation of singly and doubly coordinated hydroxyl groups. In water-poor environments, the surface is terminated exclusively by doubly coordinated hydroxyl groups.

Consistently, our VIMP data suggest that the catalytic effect exerted by hematites on the ORR (given by $I(C_{ORR})$) is larger for dehydroxylated hematite forms whereas the intensity of the C_{HE} peak ($I(C_{HE})$) is larger for hydroxylated ones but lower for hydrated ochre forms. Accordingly, the intensity of the C_{HE} process results from a compromise between accessibility of the metal centers to the oxidation and the degree of surface hydroxylation.[15–17,47–49] Accordingly, the averaged values of the $I(C_{HE})/I(C_{ORR})$ ratio can be taken as representative of the combination of the above parameters. Accordingly, in heating experiments between 300 and 700 °C the control of the Fe(IV)/Fe(III) couple is the prevailing effect so that the $I(C_{HE})/I(C_{ORR})$ ratio increases slowly with temperature for all hematites. Above 900 °C, however, the hydroxylation level decreases abruptly and the voltammetric response is dominated by the large catalytic effect exerted on the ORR process by anhydrous hematite.

Archaeometric Implications

Figure 11 shows the representation of $I(C_{ORR})$ vs. $I(C_{HE})$ recorded in SWVs in conditions such as in Figure 5 for Apulian pottery samples from a) Arpi and Taranto, and b) Altamura and Monte Sannace. Clearly, the experimental data points of samples of each site fall in separate regions of the diagram, all below the tendency line defined by anhydrous, crystalline hematite using data depicted in Figure 8.

For archaeometric purposes, it is pertinent to underline that: i) the averaged $I(C_{HE})/I(C_{ORR})$ ratios of Apulian pottery samples are clearly larger than those of anhydrous hematite H0, but close to that of hydroxylated hematites H1-H3, thus

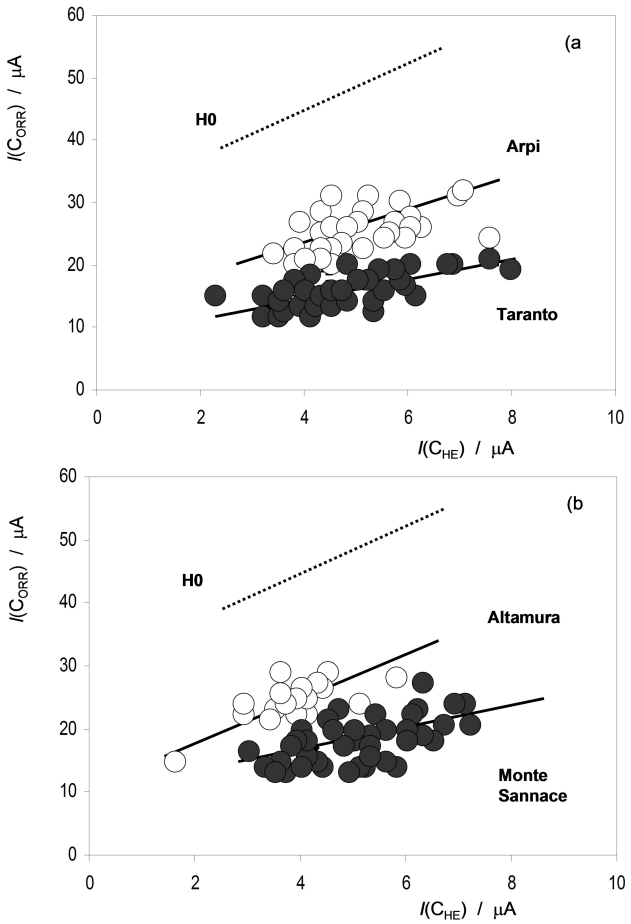

Figure 11. Plots of $I(C_{ORR})$ vs. $I(C_{HE})$ recorded in SWVs in conditions such as in Figure 5 for Apulian red-figured pottery samples from a) Arpi and Taranto, and b) Altamura and Monte Sannace accompanied by the tendency line for crystalline hematite from Figure 7.

suggesting that these specimens exhibit an equivalent electrochemical behavior; ii) the production from each archaeological site displays a characteristic voltammetric pattern. Accordingly, we can use VIMP data to characterize the production from each archaeological site using samples at the microgram level.

Identifying the A-process in Eq. (8) as the A_{HE} one and the B-process in the same equation as the hematite-catalyzed ORR, one can assume that the parameters S_o, g_A, h_A are essentially identical for all ceramic samples, whereas the p, g_B, h_B parameters will be sample-characteristic. Then, equation (10) can be rewritten as equation (11):

$$I_B(\text{site J}) = B_J I_A(\text{site J}) + C_J \quad (11)$$

where B_J and C_J represent site-characteristic parameters easily determined from the linear fit of experimental data such as in Figure 11. The corresponding values of the coefficients B_J and C_J are listed in Table 1. One can see here that, in spite of the relatively large data dispersion, there is possibility of discriminating (but also grouping) the different archaeological sites. The differences observed between distinct archaeological sites reflect the differences in raw materials and manufacturing conditions. In principle, hematite can be viewed as a temperature marker, the lower $I(C_{ORR})/I(C_{HE})$ ratios will indicate higher firing temperatures, in particular above 900 °C, but further research is needed to properly elucidate this matter.

Table 1. Values of the coefficients B_J and C_J in equation (6), characterizing the different archaeological sites. From linear fit of data such as in Figure 7 recorded in SWVs of sample-modified graphite electrodes in contact with air-saturated 0.10 M HCl solution in conditions, such as in Figure 2. *Anhydrous, crystalline hematite. *r*: correlation coefficient.

Site	B_J	C_J	*r*
Hematite*	3.9 ± 1.7	28 ± 8	0.72
Altamura	2.7 ± 0.7	13 ± 2	0.70
Arpi	2.0 ± 0.5	14 ± 3	0.52
Monte Sannace	2.0 ± 0.3	8.2 ± 1.7	0.60
Taranto	1.5 ± 0.2	9.0 ± 1.0	0.71

Conclusions

Application of VIMP and SECM techniques to microparticulate deposits of different hematite and ochre specimens in contact with air-saturated HCl solutions yields well-defined features associated to catalytic effects on ORR and OER processes. The voltammetric features, although sensitive to a variety of factors (shape and size of crystals, Al^{3+} for Fe^{3+} substitution, …) appear to be particularly dependent on the degree of surface hydroxylation of the mineral. In particular, the electrochemical response is quite sensitive to the application of firing temperatures above 900 °C. Accordingly, the relative intensity of the voltammetric signatures associated to hematite is potentially usable as a firing temperature marker in ceramic materials.

The VIMP and SECM responses of specimens from the clay body of Apulian red-figured pottery providing from the archaeological sites of Altamura, Arpi, Monte Sannace and Taranto are comparable to those of hematite specimens. Although these ceramic materials possess a considerably complex composition, the electrochemical response is apparently dominated by hematite-based processes. The voltammetric features permit the discrimination between archaeological samples from the different sites. The acquisition of site-characteristic voltammetric profiles from samples at the microgram level is of considerable potential interest for archaeometric studies.

Acknowledgments

The work was carried out within the framework of project PID2020-113022GB-I00 which was financially support by Ministerio de Ciencia e Innovación and Agencia Estatal de Investigación (AEI) of the Spanish government.

Conflict of Interest

The authors declare no conflict of interest.

Keywords: voltammetry · hematite · ceramic clays · oxygen reduction reaction · oxygen evolution reaction

[1] A. Valdés, J. Brillet, M. Grätzel, H. Gudmundsdóttir, H. A. Hansen, H. Jónsson, P. Klüpfel, G. J. Kroes, F. L. Formal, I. C. Man, R. S. Martins, J. K. Nørskov, J. Rossmeisl, K. Sivula, A. Vojvodic, M. Zäch, *Phys. Chem. Chem. Phys.* **2012**, *14*, 49.
[2] H. Zhu, S. Zhang, Y. X. Huang, L. Wu, S. Sun, *Nano Lett.* **2013**, *13*, 2947–2951.
[3] K. Shimizu, K. Tschulik, R. G. Compton, *Chem. Sci.* **2016**, *7*, 1408.
[4] K. Shimizu, L. Sepunaru, R. G. Compton, *Chem. Sci.* **2016**, *7*, 3364.
[5] H. Wan, M. Lv, X. Liu, G. Chen, N. Zhang, Y. Cao, H. Wang, R. Ma, G. Qiu, *ACS Sustainable Chem. Eng.* **2019**, *7*, 11841.
[6] J. H. Kennedy, K. W. Frese, *J. Electrochem. Soc.* **1978**, *125*, 709.
[7] K. Sivula, F. L. Formal, M. Grätzel, *ChemSusChem* **2011**, *4*, 432.
[8] L. M. Peter, *J. Solid State Electrochem.* **2013**, *17*, 315.
[9] J. R. Galán-Mascarós, *ChemElectroChem* **2015**, *2*, 37.
[10] F. Bouhjar, B. Bessaïs, B. Marí, *J. Solid State Electrochem.* **2018**, *22*, 2347.
[11] X. Fan, T. Wang, H. Xue, B. Gao, S. Zhang, H. Gong, H. Guo, L. Song, W. Xia, J. He, *ChemElectroChem* **2019**, *6*, 543.
[12] H. Saada, R. Abdallah, J.-F. Bergamini, S. Fryars, V. Dorcet, L. Joanny, F. Gouttefangeas, S. Ollivier, G. Loget, *ChemElectroChem* **2020**, *7*, 1155.
[13] T. Grygar, *J. Electroanal. Chem.* **1996**, *405*, 117.
[14] T. Grugar, *J. Solid State Electrochem.* **1998**, *2*, 127.
[15] F. Le Formal, M. Grätzel, K. Sivula, *Adv. Funct. Mater.* **2010**, *20*,1099.
[16] C. Y. Cummings, F. Marken, L. M. Peter, K. G. Upul Wijayantha, A. A. J. Tahir, *J. Am. Chem. Soc.* Soc. **2011**, *134*, 1228.
[17] C. Y. Cummings, F. Marken, L. M. Peter, A. A. Tahir, K. G. U. Wijayantha, *Chem. Commun.* **2012**, *48*, 2027.
[18] B. Klahr, T. Hamann, *J. Phys. Chem. C* **2014**, *118*, 10393.
[19] A. Doménech-Carbó, S. Sánchez-Ramos, M. T. Doménech-Carbó, J. V. Gimeno-Adelantado, F. Bosch-Reig, D. J. Yusá-Marco, M. C. Saurí-Peris, *Electroanalysis* **2002**, *14*, 685.
[20] A. Doménech-Carbó, M. A. Villegas, F. Agua, S. Martínez, M. T. Doménech-Carbó, B. Martínez, *J. Am. Ceram. Soc.* **2016**, *99*, 3915.
[21] F. Di Turo, N. Montoya, J. Piquero-Cilla, C. De Vito, F. Coletti, I. De Luca, A. Doménech-Carbó, *Appl. Clay Sci.* **2018**, *162*, 305.
[22] L. La-Torre-Riveros, A. Doménech-Carbó, C. R. Cabrera, M. T. Doménech-Carbó, W. Huahuasoncco-Condori, D. Q. Guzmán, M. C. Gutiérrez-Castillo, K. Carmona-Ochoa, A. Pérez-Trujillo, *Solid State Electrochem.* **2019**, *23*, 1541.
[23] M. Ramacciotti, G. Gallello, D. Navarro-Martos, A. Doménech-Carbó, C. Roldán, E. Hernández, S. Garrigues, A Pastor, *Appl. Clay Sci.* **2020**, *198*, artic. 105857.
[24] L. Fabrizzi, L. Nigro, F. Cappella, F. Spagnoli, M. Guirguis, A. M. Niveau de Villedry, M. T. Doménech-Carbó, C. De Vito, A. Doménech-Carbó, *Electroanalysis* **2020**, *32*, 258.
[25] F. Scholz, B. Meyer, Voltammetry of solid microparticles immobilized on electrode surfaces, in *Electroanalytical Chemistry*, A Series of Advances. A. J. Bard, I. Rubinstein, Eds., Marcel Dekker, New York, vol. 20, pp 1–86, **1998**.
[26] F. Scholz, U. Schröder, R. Gulabowski, A. Doménech-Carbó, *Electrochemistry of Immobilized Particles and Droplets*, 2nd ed. Springer, Berlin-Heidelberg, **2014**.
[27] A. Doménech-Carbó, J. Labuda, F. Scholz, *Pure Appl. Chem.* **2013**, *85*, 609.
[28] A. Doménech-Carbó, M. T. Doménech-Carbó, V. Costa, *Electrochemical Methods in Archaeometry, Conservation and Restoration* (Monographs in Electrochemistry series, F. Scholz, Ed.). Springer, Berlin-Heidelberg, **2009**.
[29] A. Doménech-Carbó, M. T. Doménech-Carbó, *Pure Appl. Chem.* **2018**, *90*, 447.
[30] A. Doménech-Carbó, F. Scolz, M. T. Doménech-Carbó, J. Piquero-Cilla, N. Montoya, T. Pasíes-Oviedo, M. Gozalbes, J. M. Melchor-Montserrat, A. Oliver, *ChemElectroChem* **2018**, *5*, 2113.
[31] B. Ramírez-Barat, E. Cano, *ChemElectroChem* **2018**, *5*, 2698.
[32] B. Ramírez-Barat, E. Cano, *ChemElectroChem* **2019**, *6*, 2553.
[33] A. Doménech-Carbó, F. Scolz, M. T. Doménech-Carbó, M. Silva, J. M. Valle-Algarra, J. V. Gimeno-Adelantado, F. Bosch-Reig, R. Mateo-Castro, *Analyst* **2015**, *140*, 1065.
[34] H. D. Ruan, R. L. Frost, J. T. Kloprogge, *Spectrochim. Acta Part A* **2001**, *57*, 2575.
[35] V. Schwertmann, R. W. Fitzpatrick, J. Le Roux, *Clays Clay Miner.* **1977**, *25*, 373–374.
[36] S. A. Fysh, P. M. Fredericks, *Clays Clay Miner.* **1983**, *31*, 377.
[37] J. L. Rendón, C. J. Serna, *Clay Miner.* **1981**, *16*, 375.
[38] M. Walton, K. Trentelman, M. Cummings, G. Poretti, J. Maish, D. Saunders, *J. Am. Ceram. Soc.* **2013**, *96*, 2031.
[39] L. Lühl, B. Hesse, I. Mantouvalou, M. Wilke, S. Mahlkow, E. Aloupi-Siotis, B. Kanngiesser, *Anal. Chem.* **2014**, *86*, 6924.
[40] E. Aloupi-Siotis, *Archaeol. Anthropol. Sci.* **2020**, *12*, 191.
[41] A. Mangone, L. C. Giannossa, A. Ciancio, R. Laviano, A. Traini, *J. Archaeol. Sci.* **2008**, *35*, 1533.
[42] J. Thorn, M. Glascock, *Archaeometry* **2010**, *52*, 777.
[43] A. Mangone, L. C. Giannossa, R. Laviano, C. S. Fioriello, A. Traini, *Microchem. J.* **2009**, *91*, 214–221.
[44] A. Mangone, L. C. Giannossa, G. Colafemmina, R. Laviano, A. Traini, *Microchem. J.* **2009**, *92*, 97.
[45] A. Mangone, M. C. Caggiani, L. C. Giannossa, G. Eramo, V. Redavid, R. Laviano, *J. Cult. Herit.* **2013**, *14*, 82.
[46] O. Henrotte, A. Boudet, N. Limani, P. Bergonzo, B. Zribi, E. Scorsone, B. Jousselme, R. Cornut, *ChemElectroChem* **2020**, *7*, 4633.
[47] H. Guo, A. S. Barnard, *J. Phys. Chem. C* **2011**, *115*, 23023.
[48] O. Zandi, T. W. Hamann, *Nat. Chem.* **2016**, *8*, 778.
[49] C. Tang, B. Sun, M. Li, J. Zhang, X. Fan, F. Gao, Y. Tong, L. Dong, Y. Li, *J. Mater. Chem. A* **2019**, *7*, 8050.
[50] M. Noked, A. Soffer, D. Aurbach, *J. Solid State Electrochem.* **2011**, *15*, 1563.
[51] Y. Yi, G. Weinberg, M. Prenzel, M. Greiner, S. Heumann, S. Becker, R. Schlögl, *Carbon* **2017**, *295*, 32.
[52] T. Grygar, P. Bezdicvka, D. Hradil, A. Doménech-Carbó, F. Marken, L. Pikna, G. Cepriá, *Analyst* **2002**, *127*, 1100.
[53] A. Doménech-Carbó, M. T. Doménech-Carbó, H. G. M. Edwards, *Electroanalysis* **2007**, *19*, 1890.
[54] M. Lovric, F. Scholz, *J. Solid State Electrochem.* **1997**, *1*, 108.
[55] K. B. Oldham, *J. Solid State Electrochem.* **1998**, *2*, 367.
[56] M. Lovric, F. Scholz, *J. Solid State Electrochem.* **1999**, *3*, 172.
[57] U. Schröder, K. B. Oldham, J. C. Myland, P. J. Mahon, F. Scholz, *J. Solid State Electrochem.* **2000**, *4*, 314.
[58] H. Guo, B. Gilbert, C. Frandsen, E. R. Maxey, D. M. Sherman, *Phys. Rev. B* **2009**, *79*, 035108.
[59] R. Jinnouchi, A. B. Anderson, *J. Phys. Chem. C* **2008**, *112*, 8747.
[60] A. B. Anderson, R. Jinnouchi, J. Uddin, *J. Phys. Chem. C* **2013**, *117*, 41.

Manuscript received: September 4, 2021
Revised manuscript received: October 12, 2021
Accepted manuscript online: October 12, 2021